ChemPubSoc Europe

DOI: 10.1002/cphc.201402417

Quinone-Rich Poly(dopamine) Magnetic Nanoparticles for Biosensor Applications

Miriam Martín,[a] Alejandro González Orive,[b] Pablo Lorenzo-Luis,[c] Alberto Hernández Creus,[b] José Luis González-Mora,[a] and Pedro Salazar*[a, d]

Novel core-shell quinone-rich poly(dopamine)–magnetic nanoparticles (MNPs) were prepared by using an in situ polymerization method. Catechol groups were oxidized to quinone by using a thermal treatment. MNPs were characterized by using X-ray diffraction, X-ray photoelectron spectroscopy, atomic force microscopy, magnetic force microscopy, UV/Vis, Fourier-transform infrared spectroscopy, and electrochemical techniques. The hybrid nanomaterial showed an average core diameter of 17 nm and a polymer-film thickness of 2 nm. The core-shell nanoparticles showed high reactivity and were used as solid supports for the covalent immobilization of glucose oxidase (Gox) through Schiff base formation and Michael addition. The amount of Gox immobilized onto the nanoparticle surface was almost twice that of the nonoxidized film. The resulting biofunctionalized MNPs were used to construct an amperometric biosensor for glucose. The enzyme biosensor has a sensitivity of 8.7 mA M^{-1} cm^{-2}, a low limit of detection (0.02 mM), and high stability for 45 days. Finally, the biosensor was used to determine glucose in blood samples and was checked against a commercial glucometer.

1. Introduction

Surface-functionalization methods are currently attracting attention in such areas as biomedical applications, biosensing, protein adsorption, biomimetic and bioactive films, biomineralization, and cell adhesion, proliferation, and differentiation.[1–9] The most common methods to carry out surface functionalization are self-assembled monolayer (SAM), electro- and photopolymerization, plasma polymerization, and layer-by-layer (LbL) deposition.[10–13] For example, LbL produces films of controllable thickness and permeability, although it involves multiple deposition steps and is time-consuming.[12–16] However, common methods may be complex, limited to certain specific surfaces, laborious, and sometimes poorly reproducible.

For biosensor construction, the effective immobilization of enzyme is the key step. Despite many advances in enzyme biosensors, it is still a challenge to search for some new materials and methods to improve their simplicity, sensitivity, selectivity, and stability. Thus, new and green functionalization approaches that allow easy and reproducible modifications are needed. Polymerization of catecholamines, such as dopamine (DA), is an important and versatile building block for the design of mussel-inspired synthetic adhesives and coating films,[17–21] which offer a new multiplatform for further derivatizations.[22–26] In addition, oxygen-assisted polymerization is very soft, without the need for any complicated equipment or severe reaction conditions as in the case of other methods (thermal and photopolymerization). Most importantly, DA polymerization in aerated basic solution forms an adherent poly(dopamine) (pDA) film over a wide variety of organic and inorganic surfaces. This wide applicability and ease of use is the reason this film has generated a growing interest and have been many reports on the use of pDA for biosensor applications.[27–32] However, the structure of this polymeric film is not yet elucidated.[33–37] The polymerization of dopamine to pDA under slightly basic conditions is probably formed by the reaction of the primary amino groups and quinone groups of oxidized DA through the formation of Schiff bases and/or Michael addition adducts. In the early stages of the study of the film, some authors suggested a mechanism pathway similar to eumelanin synthesis, but this is still a matter of scientific debate.[33,36] DA oxidation leads to dopaminochrome through a multistep reaction pathway that produces complex networks of polymers with free catechol groups. These catechol groups

[a] M. Martín, Prof. J. L. González-Mora, Dr. P. Salazar
Neurochemistry and Neuroimaging group, Faculty of Medicine
University of La Laguna, Campus de Ofra s/n
38071 La Laguna, Tenerife (Spain)
E-mail: psalazar@ull.edu.es

[b] Dr. A. González Orive, Prof. A. Hernández Creus
Physical Chemistry Area, Section of Chemistry
Faculty of Science, Institute of Materials and
Nanotechnology (IMN), Avda Francisco Sánchez s/n
University of La Laguna
38071 La Laguna, Tenerife (Spain)

[c] Prof. P. Lorenzo-Luis
Inorganic Chemistry Area, Section of Chemistry
Faculty of Science, Avda Francisco Sánchez s/n
University of La Laguna
38071 La Laguna, Tenerife (Spain)

[d] Dr. P. Salazar
Laboratory of Nanotechnology on Surfaces
Institute of Materials Science of Seville (CSIC-Univ. Sevilla)
Calle Américo Vespucio 49, 41092, Sevilla (Spain)
E-mail: psalazar@icmse.csic.es

Supporting Information for this article is available on the WWW under http://dx.doi.org/10.1002/cphc.201402417.

are responsible for the strong adhesion of the polymer network.

However, the presence of residual quinone groups allows further modification by nitrogen derivatives and thiol residues through Schiff base formation or Michael-type addition, respectively.[37] Thus, reactive quinones at the surface of pDA films may be used as anchoring points for further chemical modification and/or immobilization of biologically active macromolecules (e.g. antibodies, enzymes, aptamers, factor growths).[4,17,24,33,36–41] Taking in to account that free quinones are responsible for such immobilization, it could be interesting to increase the amount of these reactive groups in the film and thus to increase the number of anchoring points for further modifications. Thus, Luo et al.[42] (2013) showed that a quinone-rich pDA film can be obtained by using thermal oxidation; by using this approach, these authors reported a clear increase in endothelium cell proliferation and platelet adhesion.

In contrast to classical materials, nanoparticles properties with high surface area are no longer determined by their bulk, but by their nanoscale architecture, and in recent years have witnessed their applications in various fields, such as electrochemistry and catalysis.[43,44] The immobilization of enzymes on the surface of magnetic nanoparticles (MNPs) offers numerous advantages, including the enhancement of the enzymatic loading and the reduction of the mass-transfer processes. In recent years, many publications that use different approaches can be found, which shows the great interest in the scientific community.[45–49]

MNPs also provide a favorable microenvironment for electrochemical devices in which enzymes may exchange electrons directly with the transducer,[50,51] which improves the sensitivity and selectivity of electrochemical biosensors.[52] Although enzymes have been successfully immobilized onto MNPs, the expected high stability and activity still cannot be met due to the loss of enzymatic functions.[53,54]

Based on this idea, we have shown for the first time, to the best of our knowledge, that by using quinone-rich pDA films we can improve the analytical response in biosensor devices. We used iron oxide MNPs as nanosized supports for the quinone-rich pDA film. Thus, glucose oxidase (Gox) was covalently immobilized on the quinone-rich pDA-modified MNPs.

Finally, enzyme-modified MNPs were transferred onto the surface of a Prussian Blue (PB)-modified screen-printed electrode, in which the enzymatic response was studied by detecting the enzyme-generated H_2O_2 at low applied potentials.

2. Results and Discussion

The strategy used to prepare the functionalized MNPs and the Gox-based biosensor is explained in the Experimental Section and is illustrated in Figure 1.

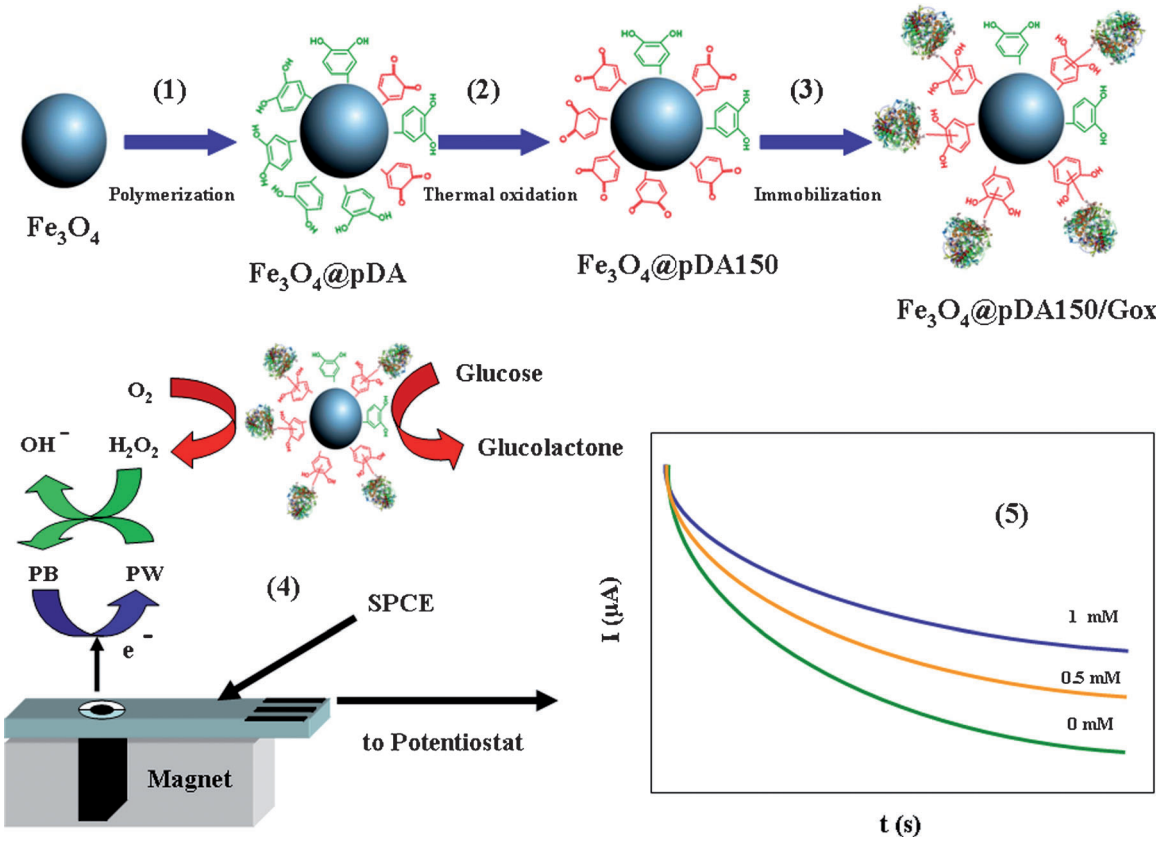

Figure 1. Schematic illustration of the synthesis of core-shell Fe_3O_4@pDA150/Gox nanoparticles and the construction of the Fe_3O_4@pDA/Gox-modified screen-printed carbon electrode (SPCE).

2.1. Characterization of Core-Shell Fe_3O_4@pDA150 Nanoparticles

2.1.1. X-ray Diffraction (XRD)

Fe_3O_4 nanoparticles, synthesized by coprecipitation of Fe^{2+}/Fe^{3+} ions in alkali media, Fe_3O_4@pDA, and Fe_3O_4@pDA150 nanoparticles were characterized by X-ray diffraction (Figure S1A in the Supporting Information). Fe_3O_4 nanoparticles showed diffraction peaks at 21.55, 30.35, 35.49, 43.39, 53.90, 57.41, and 62.90°, which correspond to the (111), (220), (311), (400), (422), (551), and (440) Bragg reflections, respectively. This pattern confirmed the polycrystalline nature of Fe_3O_4 with a cubic spinel structure. The presence of very broad peaks indicated the ultrafine nature and small crystallite size of the nanoparticles. Thus, the crystallite size was calculated by using the Debye–Scherrer equation and the full-width at half diffraction (FWHM) value of the (331) XRD diffraction line, and presented a value of 17.2 nm. The lattice parameter (a) and interplanar spacing (d_{hkl}) were determined by using Bragg's law and were found to be 8.400 and 2.529 Å, respectively, which are very close to the reported values for pure magnetite (8.394 and 2.531 Å, respectively).[55] The X-ray photoelectron spectroscopy (XPS) analysis (see Section 2.1.2) was also used to determine the atomic ratio of iron and oxygen, which was approximately 0.8, which is close to the theoretical value of 0.75 and verifies the formation of Fe_3O_4. A similar XRD pattern was observed for the polymer-modified core-shell nanoparticles (Figure S1B), which suggests that the crystalline structure of the nanomaterial was not affected by coating with the polymer thin film. To obtain a quinone-rich pDA-film, MNPs were heated at 150 °C for 1 h and changed to a rusty color, probably due to the oxidation of the external shell and the generation of a γ-Fe_2O_3 shell on the MNP surface. Nevertheless, XRD did not show any change (Figure S1C), because the XRD patterns of magnetite (Fe_3O_4; JCPDS card 75-0449) and maghemite (γ-Fe_2O_3; JCPDS card 39-1346) are almost identical.[56] Additional analysis techniques were performed to characterize this phase transition and the catechol/quinone conversion after thermal treatment.

2.1.2. XPS

XPS was used to examine the shell structure of these nanoparticles because core electron lines of ferrous and ferric ions can be detected and distinguished by using this technique. Figure 2A shows the results of the XPS spectrum of Fe_3O_4@pDA, thus magnetite was confirmed according to the typical characteristic peaks of Fe $2p_{3/2}$ and Fe $2p_{1/2}$ at 710.9 and 724.5 eV, respectively.[56] A relatively weak peak for Fe 3p line at 55.9 eV was also detected. C 1s and N 1s peaks at 284.6 and 398.9 eV, respectively, confirmed the polymerization of pDA onto the MNP surface. The detailed spectra for Fe $2p_{3/2}$, Fe $2p_{1/2}$, and O 1s were investigated to obtain a more detailed study of the processes that occur during thermal oxidation. After heat treatment, the peak position of Fe $2p_{3/2}$ and Fe $2p_{1/2}$ bands shifted to a lower binding energy by about 1 eV and confirmed the phase transition from magnetite (Fe_3O_4) to maghemite (γ-Fe_2O_3; Figure 2B).[57] This conversion probably occurs on the external shell of the nanoparticle and the core is still Fe_3O_4, which is why we continue to use this nomenclature after thermal oxidation (Fe_3O_4@pDA150).

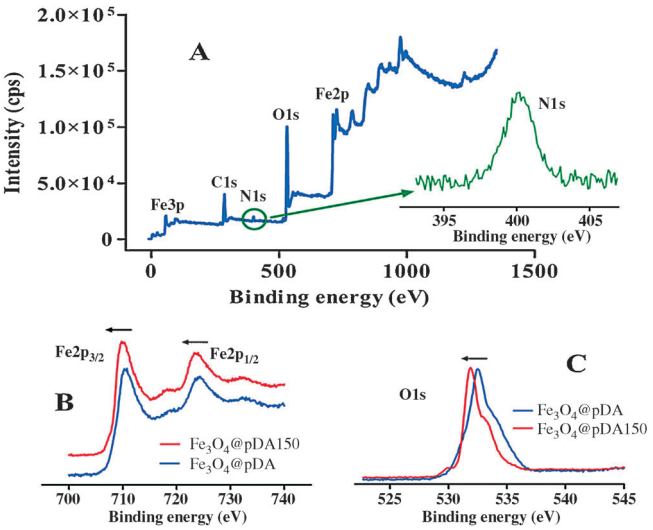

Figure 2. A) XPS spectra of Fe_3O_4@PDA core–shell MNPs. Inset: The expanded spectrum of the N 1s core line. B) High-resolution XPS spectra of Fe $2p_{3/2}$ and Fe $2p_{1/2}$ core-level lines for Fe_3O_4@PDA and Fe_3O_4@PDA150. C) High-resolution XPS spectra of O 1s core-level lines for Fe_3O_4@PDA and Fe_3O_4@PDA150.

This affirmation is based on previous publications in which other authors found that Fe_3O_4 nanoparticles were only partly transformed into γ-Fe_2O_3 under 200 °C for 3 h and needed a temperature of 600 °C for 3 h to completely transform into Fe_2O_3.[58] Figure 2C shows the high-resolution spectra for O 1s in Fe_3O_4@pDA and Fe_3O_4@pDA150, in which a clear shift to lower binding energies is also observed after thermal treatment. This observation has been justified by other authors as a result of the greater contribution from the quinone (C=O, 531.4 eV) than the catechol (C–OH, 533.0 eV) groups in the biofilm after thermal oxidation.[42] Finally, the high-resolution spectra for O 1s were deconvoluted (Figure S2). The peak centered at 530.5 eV was assigned to the Fe–O lattice, whereas the other two peaks at approximately 531.5 and 533 eV were assigned to C=O and C–OH groups, respectively. The quinone/catechol ratio was determined and revealed a quinone contribution of approximately 60%. This value is two times higher than the amount reported by Luo et al.[42] for unmodified films and it is in good agreement with data reported for thermally oxidized films (≈50%) by these authors.

2.1.3. Atomic Force Microscopy (AFM)

Typical AFM images of the highly oriented pyrolytic graphite (HOPG) surfaces immersed in the three different MNP-containing solutions are shown in Figure 3. The images show the formation of granular deposits formed by aggregated nanoparticles that partially cover the substrate surface. It should be noted that, even for the larger aggregates, individual particles can be easily detected as building blocks, which confirms that

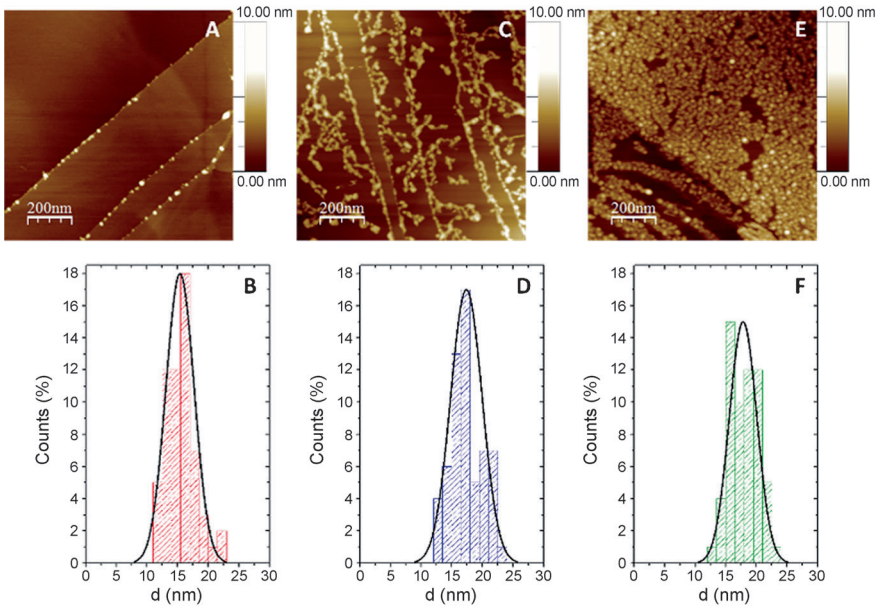

Figure 3. Top: Typical 1.0×1.0 μm^2 AFM images recorded for A) Fe_3O_4, C) Fe_3O_4@PDA, and E) Fe_3O_4@PDA150 particles adsorbed on HOPG. Bottom: Histograms showing particle size distributions for B) Fe_3O_4, D) Fe_3O_4@PDA, and F) Fe_3O_4@PDA150.

they still conserve their singularity and have not sintered. Uncovered MNPs tend to adsorb (physisorption) mainly at HOPG steps, whereas the basal plane remains practically unaltered, as can be seen in Figure 3A. The size distribution is presented as a histogram in Figure 3B and summarized in Table S1. After modification with the PDA film (Figure 3C), MNPs still decorate HOPG steps although it can be observed that these particles spread out to the HOPG terraces and start to aggregate, which gives rise to ramified islands. By comparing the averaged sizes registered before and after modification with the biopolymer (Figure 3B and D and Table S1), it can be concluded that the PDA film thickness is approximately 1 to 2 nm, which is in good agreement with the High-resolution transmission electron microscopy (HRTEM) data (Figure S3). Interestingly, after the heat treatment, the ramified islands seemed to collapse and form an almost complete particle monolayer on the HOPG surface (Figure 3E). The histogram depicted in Figure 3F exhibited no significant differences to that obtained before the thermal treatment. The mechanisms involved in the formation of the MNP films will be clarified below. Naked magnetite nanoparticles are mainly found at defects and steps of the HOPG.

It should be noted that contributions from electrostatic interactions and hydrogen bonding could play a key role at HOPG step edges, at which different types of functional groups are present, which thus explains the preferential adsorption at these defects compared with the mostly inert basal plane.

However, the 2D arrangement shown by Fe_3O_4@pDA (Figure 3C) and Fe_3O_4@pDA150 (Figure 3E) can be justified in terms of the π–π interactions that exist between the basal plane of graphite and the aromatic subunits located at the surface of MNPs, and this arrangement is significantly enhanced by the contribution from the increased rate of aromatic quinone due to the thermal treatment.

Therefore, the heating treatment not only markedly contributes to the efficient chemisorption of Gox onto the MNP surfaces, but it also collaborates in the selective adsorption on the highly hydrophobic and inert basal plane of HOPG. This strategy could also be applied to modify other graphitic-like surfaces, such as carbon nanotubes (CNTs) and reduced graphene oxide (RGO).[59,60]

2.1.4. Magnetic Force Microscopy (MFM)

As reported elsewhere, MFM is a valuable technique that can be used to detect, characterize, and identify magnetic domains present in the sample, in particular those defined by the assembly of MNPs.[61,62] In fact, MFM imaging has been successfully used to characterize the magnetic properties shown by bidimentional self-assembled melanin–iron biofilms and Ni-aggregated nanoparticles both supported on a HOPG basal plane.[63,64]

In this context, the size of the magnetic particle is a significant factor that has a surprisingly strong effect on its magnetic properties. Thus, magnetite particles ranging from 35 to 80 nm in diameter must be considered to be single-domain magnets.[65]

However, magnetite particles with diameters below 30 nm seem to exhibit superparamagnetic behavior because they do not have sufficient volume to ensure a stable magnetic moment and, therefore, thermal energy can reverse the magnetic moment.[66]

Taking into account the diameter values expressed as histograms and collected in Table S1, the range of the magnetite nanoparticles described here should correspond to superparamagnetic particles. Images that show topographic, phase contrast, and magnetic phase contrast features (registered at 50 nm above the sample), are shown in Figure 4A–C, respectively. Figure 4A and B exhibits a clear correspondence between the presence of the aggregated nanoparticles and dark zones related to them in the phase contrast image, whereas the unmodified HOPG basal plane clearly corresponds to the bright zones. However, Figure 4C shows globular-like magnetic domains of a few hundred nanometers that show alternated phase contrast, that is, dark and bright phase contrast areas (highlighted with blue and red dashed circles), which are attributed to attractive and repulsive interactions between tip and sample, respectively. Indeed, the red and blue circles indicate different regions with similar morphological and phase

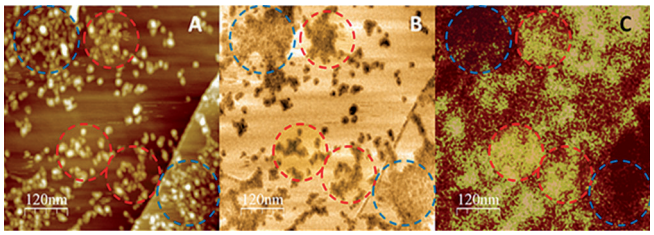

Figure 4. Typical 600×600 nm^2 MFM images recorded for Fe_3O_4@pDA150 adsorbed on HOPG. A) Topographical image, B) contrast phase image, and C) contrast phase image at lift scan height of 50 nm. Blue and red dashed circles indicate MNP aggregates that show different magnetic phase contrast: darker areas are negative and brighter areas are positive.

contrast features (Figure 4A, B), but an opposed magnetic phase contrast (Figure 4C) formed by aggregated nanoparticles that exhibit parallel magnetization. Analogue ferromagnetic-like behavior due to the 2D assembly of these functionalized magnetite nanoparticles has also been observed for assemblies of 12 nm nanoparticles that consist of a core of Co surrounded by a 1 nm shell of oleic acid on Si.[67]

3.2. Enzymatic Immobilization onto Core-Shell Fe_3O_4@pDA150 Nanoparticles

3.2.1. UV/Vis Spectroscopy

The immobilization step was studied by using UV/Vis spectroscopy.[52] In this sense, UV/Vis analyses were done for each component (Fe_3O_4, pDA, and Gox) and for the final modified nanoparticles (Fe_3O_4@pDA150/Gox), and the results are shown in Figure 5A. The enzyme solution presented a characteristic adsorption band at around $\lambda = 264$, 355, and 450 nm, whereas the pDA solution showed a typical adsorption band around $\lambda = 310$ nm that resulted from the formation of the quinone intermediate and the polymerized film. The surface modification of the Fe_3O_4 nanoparticles with these adducts can be confirmed by comparing the spectra of the raw and modified nanoparticle solutions. UV/Vis analysis of Fe_3O_4@pDA150/Gox samples revealed that two peaks at $\lambda = 260$ and 310 nm were superimposed on the characteristic broad adsorption peak of Fe_3O4 nanoparticles, which suggested that the nanoparticles were successfully covered with the pDA film and further modified with the Gox enzyme.

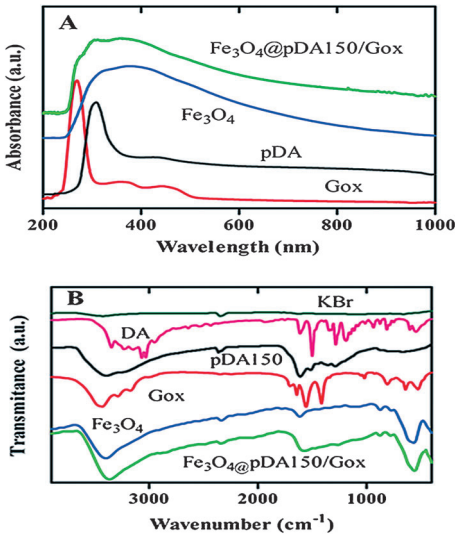

Figure 5. A) UV/Vis adsorption spectra of free Gox, pDA, Fe_3O_4, and Fe_3O_4@pDA150/Gox nanoparticle solutions. B) FTIR transmittance spectra of KBr, DA, pDA150, Gox, Fe_3O_4, and Fe_3O_4@pDA150/Gox nanoparticles.

At this point, we quantified the amount of Gox immobilized covalently onto different MNP configurations. Our optimized bio-nanoparticles (Fe_3O_4@pDA150/Gox) were compared with two other configurations in which 1) Gox was directly adsorbed onto the MNP surface through the combined contribution of electrostatic interactions, hydrogen bonding, Van der Waals forces, and hydrophobic interactions (Fe_3O_4/Gox); 2) Gox was covalently attached to the pDA-modified MNP surface without thermal oxidation of catechol groups to quinone (Fe_3O_4@pDA/Gox). Thus, the amount of the Gox retained on the nanoparticle surface was calculated as the difference between the initial and final enzymatic concentration in the enzymatic solution after the immobilization step onto the MNP surface.

Visible spectra (Figure S4) obtained for all configurations presented a decrease at $\lambda = 450$ nm due to the immobilization of Gox, with this change being more noticeable for the Fe_3O_4@pDA150/Gox configuration and confirming the excellent immobilization properties of the quinone-rich film.

The amount of immobilized enzyme was estimated to be approximately 21, 32, and 55 μg mg^{-1} supports for Fe_3O_4/Gox, Fe_3O_4@pDA/Gox, and Fe_3O_4@pDA150/Gox, respectively.

3.2.2. IR Spectroscopy

A more detailed study was done by using Fourier-transform infrared (FTIR) spectroscopy. Figure 5B shows spectra for each individual component (Fe_3O_4, DA, pDA150, and Gox) and for the final modified nanoparticles (Fe_3O_4@pDA150/Gox). DA shows relatively broad and strong bands in the 3000 to 3400 cm^{-1} region, assigned to the aromatic O–H asymmetry stretching vibration of CH_2 groups. Other peaks worth mentioning are found at 1602 (overlap of C=C resonance vibrations in aromatic ring) and 1519 cm^{-1} (N–H scissoring vibrations). Interestingly, the C=C resonance was enhanced and widened whereas the peak related to N–H scissoring vibrations at 1519 cm^{-1} became weaker for pDA150. Some authors have hypothesized that, during thermal treatment, intramolecular cyclization occurs and forms indole derivatives, which lead to enhanced peak intensity at 1602 cm^{-1} and decreased peak intensity at 1519 cm^{-1}.[68] Furthermore, the decreased 1519 cm^{-1} peak might also be ascribed to the oxidation of primary amino groups under thermal conditions (Figure S5). Moreover, the spectra for pDA150 also display a large relative absorbance in the 1500 to 1100 cm^{-1} region, which is attributable to substantial C–O and C–N functional groups.[42,68] FTIR spectra of Fe_3O_4 nanoparticles showed a main adsorption band at around 580 cm^{-1}, which corresponds to the Fe–O stretching modes of

the magnetite.[52] Furthermore, Fe_3O_4@pDA150/Gox nanoparticles showed an additional band in the range of 1000 to 1700 cm^{-1}, which may be ascribed to 1) the aromatic rings of pDA (1614 cm^{-1}), 2) the amide I and amide II stretching bands (1639, 1535 cm^{-1} respectively), or 3) a broad adsorption band around 1200 cm^{-1} ascribed to the C–N stretching in the new Schiff bases formed during pDA polymerization and enzymatic immobilization.[6,69]

3.3. Characterization of the Core–Shell Fe_3O_4@pDA150/Gox-Based Biosensor

To study the analytical application of the magnetic core-shell Fe_3O_4@pDA150/Gox nanoparticles, they were transferred onto the surface of a Prussian Blue (PB)-modified screen-printed electrode by using a neodymium magnet on the bottom part of the working electrode. Cyclic voltammetry (CV) in the absence of glucose (Figure S6A) displayed a well-defined cathodic and anodic peak centered about −50 mV, which corresponded to the PB↔Prussian White (PW) transition [Eq. (1)]:[70,71]

$$\{Fe_4^{III}[Fe^{II}(CN)_6]_3\}_{(PB)} \xrightarrow{4e^- + 4K^+} \{K_4Fe_4^{II}[Fe^{II}(CN)_6]_3\}_{(PW)} \quad (1)$$

An increase in the concentration of glucose systematically enhanced the cathodic current (Figure S6B), whereas the anodic current displayed a parallel decrease (Figure S6C). This observation indicates a catalytic reduction reaction that can be ascribed to the reduction of the enzyme-generated H_2O_2 to water, as previously reported.[70,71]

The dependence of the peak currents on the scan rate (Figure 6B) and the square root of the scan rate (Figure 6C) were also studied. In this way, the biosensor was cycled in the presence of 1 mM glucose from 25 to 1000 mV s^{-1} (Figure 6A). The present analysis showed that the anodic and cathodic current peaks were linearly proportional to the $v^{1/2}$ value, which is expected for a diffusion-controlled process.[72]

Figure 7 shows the chronoamperograms and the calibration curves obtained for 0.0 to 16 mM glucose (in phosphate buffer solution (PBS), pH 7.4, $E_{app} = -0.10$ V) by using our nonoptimized DPR-700/Fe_3O_4@pDA150/Gox configuration. Data showed a linear dependence at low glucose concentrations and saturation at high concentrations, in agreement with the Michaelis–Menten kinetics.[73]

3.3.1. Optimization of Different Parameters and its Effect on the Biosensor Response

Certain important parameters were studied to optimize the biosensor response (DPR-700/Fe_3O_4@pDA150/Gox).

3.3.1.1. Potential Work

The effect of the applied potential on the amperometric response of the enzyme electrode against 1 mM glucose was evaluated in the range from −300 to 200 mV (Figure S7A).The choice of applied potential at the working electrode is fundamental to achieve the lowest detection limit and to avoid the possibility of interference in biosensor applications, such as ascorbic and uric acid that are present in biological samples. The biosensor showed a practically constant and higher current value from −300 to −150 mV, the cathodic current was then decreased steadily by increasing the applied potential, and reached a value close to zero at 200 mV. This behavior agrees with the CV data discussed above and with the electrocatalytic behavior reported previously for PB-modified electrodes.[70,73] In view of these results, −150 mV was selected as the optimum value for the applied potential.

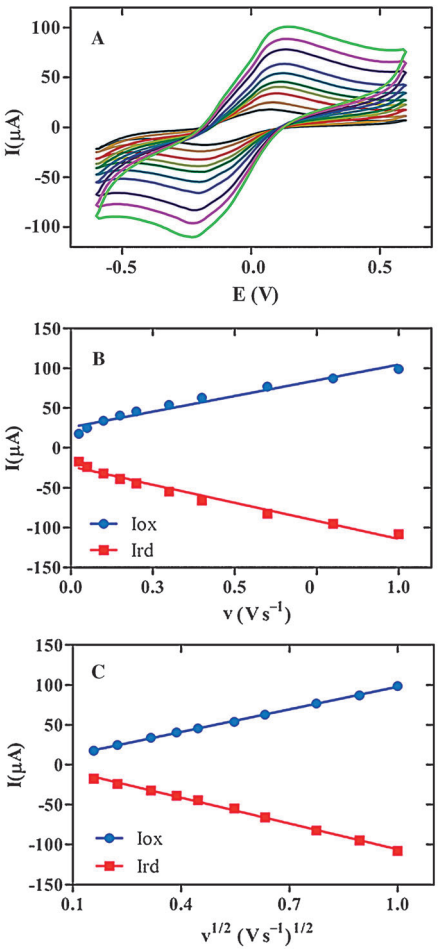

Figure 6. A) Cyclic voltammograms of DPR-700/Fe_3O_4@pDA/Gox at different glucose concentrations. B) Detail of the cathodic current peak and C) the anodic peak against scan rate.

3.3.1.2. MNP Loading

The amount of loaded nanoparticles during the preparation of the enzyme electrode was optimized to achieve the maximum sensitivity for the amperometric biosensor. The effect on the amperometric signal of the modified-magnetic beads amount immobilized on top of the working electrode surface is shown in Figure S7B. As can be seen, an increase in the amperometric signal was observed up to 60 μg and the signal decreased for higher loadings, which was probably due to an increase in the

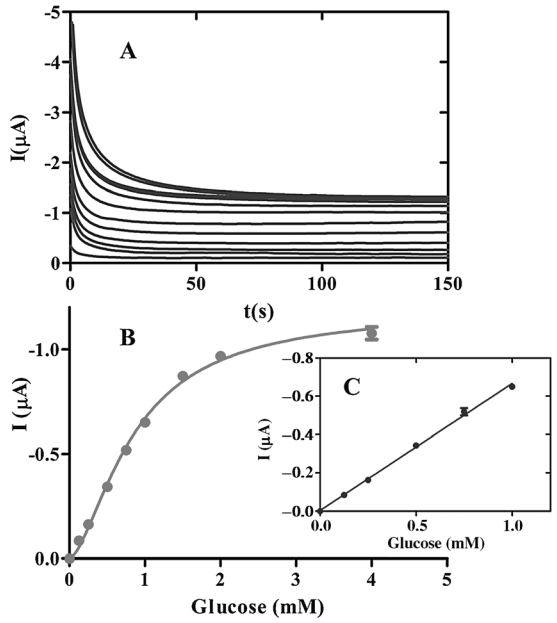

Figure 7. A) Chronoamperograms obtained for 0.0–16 mM glucose (in PBS, pH 7.4) with DPR-700/Fe_3O_4@pDA150/Gox ($E_{app} = -0.15$ V). B) Calibration curve and linear fitting (inset) obtained for the previous data (Fig. 7A).

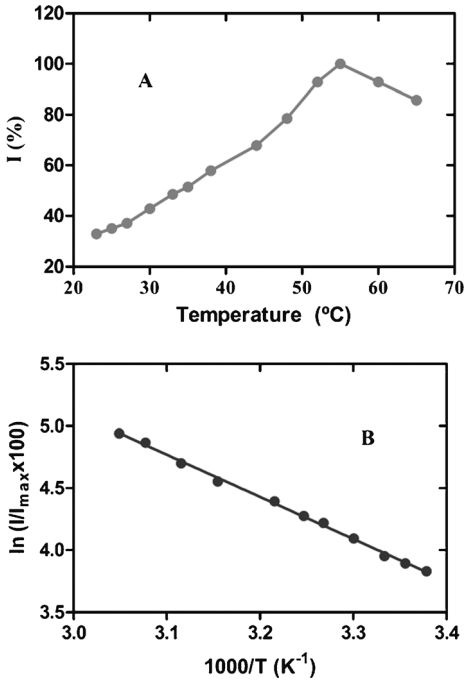

Figure 8. A) Dependence of the temperature on the current response for 0.5 mM glucose (in PBS, pH 7.4) with DPR-700/Fe_3O_4@pDA/Gox. B) Semi-log Arrhenius-type plot obtained for the previous data (Fig. 8A).

electron transfer resistance for large modified-magnetic-bead loadings; thus, 60 μg was fixed during the present study.

3.3.1.3. Effect of pH

The effect of pH on the amperometric response of the biosensor was also checked in the range of pH 5.0 to 9.0 (Figure S8A). The biosensor current exhibited an almost bell-shaped behavior, with the highest response at pH 7.4, although the signal only decreased by 15% close to the extreme values, which shows good enzymatic stabilization.

3.3.1.4. Temperature

Temperature is an important factor that affects the activity of the immobilized enzyme and thus the sensitivity of the biosensor. Therefore, the effect of temperature on the biosensor response was evaluated from 20 to 70 °C with 0.5 mM glucose in PBS. The response current increased with a rise in temperature, as shown in Figure 8A, and reached a maximum value at 55 °C, which may result from an increase in the activity of the immobilized Gox with the increase in temperature. The enzyme activity decreased over 55 °C due to the deactivation of Gox. The apparent activation energy was calculated according to the Arrhenius Equation [Eq. (2)]:

$$\ln k = \ln A - \frac{E_a}{RT} \quad (2)$$

in which k is the rate constant, E_a is the activation energy, A is the frequency factor, R is the universal gas constant, and T is the absolute temperature. As the steady-state current (i) is proportional to the rate constant k, the Arrhenius formula can be expressed as [Eq. (3)]:

$$\ln i = \ln i_0 - \frac{E_a}{RT} \quad (3)$$

Thus, the apparent activation energy, calculated from the slope of Figure 8B, was found to be 28.27 kJ mol^{-1}, which is similar to the values of 26.52 and 28.9 kJ mol^{-1} obtained by previously by Bhatti and Saleem, and Odebunmi and Owalude.[74,75] It is clear from the Arrhenius plot (Figure 8B) that Gox has a single conformation up to the transition temperature.

3.3.2. Biosensor Sensitivity for the Optimized Configuration and Comparison with Other Biosensor Configurations

After improving the enzymatic loading with respect to other MNP configurations and the biosensor response, the next step was to demonstrate the benefit of the quinone-rich film-modified MNPs on the analytical properties of our biosensor.

Consequently, our optimized configuration, DPR-700/Fe_3O_4@pDA150/Gox (**1**), was compared against three other configurations: DPR-700/Fe_3O_4@pDA/Gox (**2**), DPR-700/Fe_3O_4/Gox (**3**), and DPR-700/Gox (**4**), in which Gox was directly adsorbed onto the DRP-700 screen-printed electrode (Figure S9A and S9B). Thus, the analytical parameters, such as sensitivity, limit of detection (LOD), limit of quantification (LOQ), linear range (LR), and other enzymatic parameters, were compared (data are summarized in Table 1).

Table 1. Enzyme kinetic and analytical parameters of different glucose biosensor designs. Sensitivity was obtained in the range of 0–1 mM, mean ± SD ($n = 4$ biosensors). The limit of detection and limit of quantification were calculated as 3×SD and 10×SD of the background current, respectively. Calibration curves were obtained by applying −0.15 V against the pseudoreference electrode in air-saturated PBS (pH 7.4)

Biosensor[a]	Sensitivity [mA M^{-1}·cm^{-2}]	r^2	LOD [mM]	LOQ [mM]	K_M [mM]	V_{max} [μA]
1	8.74 ± 0.35	0.998	0.020	0.067	1.713	2.787
2	5.54 ± 0.17	0.997	0.064	0.212	1.752	1.757
3	2.38 ± 0.41	0.998	0.149	0.496	1.741	1.172
4	0.91 ± 0.16	0.996	0.282	0.942	2.773	0.426

[a] Biosensors denoted as **1**: DPR-700/Fe_3O_4@pDA150/Gox, **2**: DPR-700/Fe_3O_4@pDA/Gox, **3**: DPR-700/Fe_3O_4/Gox, and **4**: DPR-700/Gox.

All biosensors presented a linear range up to 1 mM, and DPR-700/Fe_3O_4@pDA150/Gox (**1**) showed the highest sensitivity of approximately 8.7 mA M^{-1} cm^{-2}, which is almost one order of magnitude greater than the DPR-700/Gox configuration and a LOD (S/N = 3) of 0.02 mM. This sensitivity is in the same range as other biosensors reported in the bibliography, in which Gox was immobilized on titanium-containing MCM-41-modified screen-printed electrodes (5.4 mA M^{-1} cm^{-2}).[76] Gox was immobilized in a composite film of poly(*o*-aminophenol) and carbon nanotubes (11.4 mA M^{-1} cm^{-2}),[77] in which Gox and HRP were immobilized in a bienzyme electrode based on a redox clay matrix (14.9 mA M^{-1} cm^{-2}).[78] The other two configurations (DPR-700/Fe_3O_4@pDA/Gox (**2**) and DPR-700/Fe_3O_4/Gox (**3**)) showed lower sensitivity and higher LODs and LOQs. These differences may be justified by taking into account the high reactivity of the quinone-rich film and the different enzymatic loading for each configuration reported above. Finally, DPR-700/Gox (**4**) showed the worst sensitivity and LOD due to its low enzymatic loading (see below).

3.3.3. Enzymatic Characterization of the Glucose Biosensor

The apparent Michaelis–Menten constant (K_{Mapp}), which indicates the enzymatic affinity for glucose, was calculated from the electrochemical version of the Lineweaver–Burk equation for each configuration [Eq. (4)]:[79]

$$\frac{1}{I_{ss}} = \frac{1}{I_{max}} + \frac{K_{Mapp}}{I_{max}} C \qquad (4)$$

in which I_{ss} is the steady-state current after the addition of substrate, C is the bulk concentration of the substrate, and I_{max} is the maximum current. K_{Mapp} values for all configurations were lower than the values reported for the free enzyme (20–30 mM).[80] However, the figures for Gox entrapped in polypyrrole films (19.0 mM)[81] and Gox in Nafion film (14.9 mM)[82] suggested that the enzymatic immobilization had no detrimental effect on enzyme affinity. Nanostructured configurations presented better affinities (≈1.7 mM) than DRP700/Gox configuration (≈2.7 mM), which confirmed the beneficial effect, the enhancement in enzymatic loading, and the reduction in the mass-transfer processes. Those values were close to data reported previously for Gox immobilized on gold/pDA-modified MNPs (1.67 mM)[29] and smaller than for Gox immobilized on highly ordered polyaniline nanotubes (2.37 mM).[83] Finally, the V_{max} value (calibration plateau or maximum current measured under saturated substrate conditions) for all configurations was also evaluated. This is an excellent parameter to evaluate the total amount of Gox immobilized in the different configurations.

Likewise, Table 1 shows a notable difference in the enzymatic loading between the nanostructured systems and the DPR-700/Gox configuration, in which Gox was directly adsorbed on the SPE surface. In the same way, the use of pDA improves the enzymatic loading on the MNP surface compared with the Fe_3O_4/Gox configuration, and presented a higher value when highly reactive quinone-rich film-modified MNPs were used.

Finally, we checked the linear correlation between the estimated amount of immobilized enzyme with the spectroscopy approach (see Section 3.2.1) and the V_{max} value obtained experimentally after biosensor calibration for each configuration. Surprisingly, the data showed a high coefficient of determination ($r^2 = 0.998$), which confirms the excellent correlation between the two methods.

3.3.4. Interference Studies and Reproducibility of the Biosensor

Reducing agents present in biological samples may be electrochemically oxidized and interfere with the detection of glucose. Thus, the biosensor's response against physiological interferences, such as ascorbic acid (AA) and uric acid (UA), was studied. Different glucose solutions were prepared with 5 mM glucose in the absence and presence of AA (100 μM), UA (300 μM), and both AA and UA (glucose and interference concentrations were selected to be close to their respective concentrations in blood samples). The solutions were then diluted in PBS (1:10) to obtain a glucose concentration in the linear range of the biosensor. Data showed only reasonably small interference of between 1 and 3% (Figure S8B), within the range of uncertainty (see below), which confirms the excellent ability of Prussian Blue to detect enzyme-generated H_2O_2 at low potential at which common interferences in clinical analysis are not easily reduced or oxidized.

The reproducibility and repeatability of the optimized biosensor (DPR-700/Fe_3O_4@pDA150/Gox) was conducted by calculating the sensitivity against glucose across a concentration range of 0 to 1 mM. The relative standard deviation (RSD) for a series of five successive measurements was 4.63% (repeatability) and for five individual biosensors was 7.37% (reproducibility). These values showed that the present approach is highly reproducible for biosensor construction.

3.3.5. Measurement of Glucose in Blood

The analytical usefulness of our enzyme-modified MNPs was demonstrated and evaluated by determining the glucose con-

centration in blood samples. One volunteer measured his glucose concentration, after biosensor calibration, by depositing a drop of blood (diluted 1:10 in PBS) onto the working, pseudoreference, and counter electrodes ($n=5$). Taking into account the factor dilution, the glucose concentration was found to be (6.25 ± 0.54) mM (mean $\pm$ SD). This value was confirmed by using a commercial glucometer (OneTouch® UltraEasy®, LifeScan). The same volunteer measured his glucose levels five times after blood extraction by depositing a drop of blood on the commercial sensor, with this value being (6.35 ± 0.42) mM. Based on these results, no significant difference was found using the two above-mentioned devices ($p=0.7522$).

In another experiment, six volunteers measured their glucose concentration using both devices (Table 2). On this occasion, the glucose values found ranged from 4 to 8 mM. These variations in the results may be justified because three volunteers measured their glucose level without having had breakfast (low glucose level); another two tested 1 h after breakfast (middle values), and one volunteer (higher value) tested 1 h after a full lunch. Finally, recovery of our DPR-700/Fe_3O_4@pDA150/Gox biosensor compared with the commercial glucometer were satisfactory (96–102%) and presented a high coefficient of determination ($r^2=0.983$). Thus, these results confirmed the potential application of our biosensor to measure glucose in real complex samples, such as blood.

Table 2. Determination and comparison of glucose in blood samples against a commercial glucometer.

Volunteer	One Touch	Biosensor[a]	Recovery [%]
1	4.83	4.68	96.89
2	4.93	4.75	96.35
3	5.12	5.11	99.80
4	6.12	6.20	101.31
5	6.15	5.93	96.42
6	6.86	7.02	102.33

[a] DPR-700/Fe_3O_4@pDA150/Gox (**1**).

3.3.6. Stability of Biomagnetic Nanoparticles

The storage stability of the Fe_3O_4@pDA150/Gox nanoparticles (stored in PBS, pH 7.4, 4 °C) was investigated in 1 mM glucose. Figure S10 shows the control chart with the central value set as the mean value of the five measurements carried out on the first day, and the upper and lower limits of control as three times the standard deviation of the central value ($\pm$3 SD). Even after storage for 45 d, the DPR-700/Fe_3O_4@pDA150/Gox biosensor did not show significant loss in amperometric response, which confirms that the quinone-rich pDA film may be suitable for a long storage period because it stabilizes the enzyme conformation and prevents its denaturation.

4. Conclusions

This work describes the first amperometric magneto-biosensor for the specific and sensitive detection of glucose based on quinone-rich pDA-modified MNPs. An easy method to modify MNPs and to increase the amount of quinone groups by using thermal oxidation is presented. This quinone-rich film may be used to immobilize further bioactive molecules, such as antibodies and enzymes.

The present approach shows that the amount of Gox immobilized is almost two times higher compared with nonoxidized films and, thus, its sensitivity and LOD were improved. Modified and unmodified MNPs were characterized and enzymatic immobilization was studied in detail. To improve the biosensor response, certain experimental variables were optimized. Physiological interference was minimized, due to the low potential applied during the enzymatic transduction.

Finally, the applicability of the biosensor was assessed by the determination of glucose in blood samples and checked against a commercial glucometer.

Experimental Section

Glucose oxidase (Gox) from *Aspergillus niger* (EC 1.1.3.4, Type VII-S), purchased as a lyophilized powder, $FeCl_3$, $FeSO_4{\cdot}7H_2O$, NaOH, and dopamine (DA) were obtained from Sigma and used as supplied. Electrochemical experiments were performed in 10 mM phosphate, 2.7 mM KCl, 137 mM NaCl, pH 7.4 buffer solutions (PBS). DA solution was prepared in PBS (adjusted at pH 8.5). Stock solutions of glucose (250 mM) were prepared in water, left for 24 h at RT to allow equilibration of the anomers, and then stored at 4 °C. PB screen-printed carbon electrodes (DPR-710) were purchased from DropSens. Electrochemical measurements were performed by using a DRP-STAT200 potentiostat and data were acquired by using Dropview software (DropSens). Transmittance spectra (UV/Vis) were recorded by using two different spectrophotometers in the range of $\lambda=200$–1000 nm with respect to water in a Transpec®-photodiode array spectrophotometer and in the range of $\lambda=320$–700 nm in a Benchmark Plus microplate spectrophotometer (Bio-Rad). The first one was used to obtain a better characterization of the modified MNPs by using a higher spectral range. However, the second one (with a microplate system with 200 μL each one) at $\lambda=450$ nm was employed to determine the amount of immobilized enzyme with a higher accuracy due to the low volume of solution employed ($\approx$1.5 mL). FTIR spectra were recorded with respect to air by using a Varian 670-IR spectrophotometer in the range 4000–400 cm^{-1}. X-ray diffraction (XRD) patterns were recorded by using a Philips Panalytical X'Pert powder diffractometer with $Cu_{K\alpha}$ ($\lambda=1.540$ Å) radiation. The XPS spectra were collected by using an ESCALAB 250 spectrometer with monochromatized $Al_{K\alpha}$ X-ray radiation ($h\nu=1486.6$ eV).

All binding energies are reported with reference to the binding energy of the C 1s core level spectrum, which corresponds to the containment carbon at 284.6 eV.

HRTEM was performed by using a JEOL JEM-3000 F microscope. Imaging to characterize both the dimensions and magnetic properties of functionalized magnetite nanoparticles was performed by using atomic force microscopy (AFM) and magnetic force microscopy (MFM), respectively. Highly oriented pyrolytic graphite (HOPG) substrates were immersed in different magnetic-nanoparticle-containing Milli-Q water solutions for 30 min. The resulting nanoparticle-modified HOPG surfaces were then removed from the solution, carefully rinsed with Milli-Q water, and dried under nitrogen before characterization. Samples were imaged by using AFM

operating in tapping mode in air with a Multimode microscope and a Nanoscope V control unit from Bruker at a scan rate of 1.0–1.2 Hz. To this end, etched silicon tips (RTESP, 271–311 kHz and 40–80 N m^{-1}) were used. MFM images were performed by interleaving the topographic scan (operating in soft tapping conditions) with the "Lift mode" scan. Images were taken at a scanning rate of 1 Hz with tips coated with magnetic CoCr film (MESP, 1–5 N m^{-1}) working at a drive frequency of ≈75 kHz. PB-modified screen-printed (DPR-700) electrodes were used as a conventional three-electrode system for CV and chronoamperometry (CA) analyses. These electrodes incorporate a conventional three-electrode configuration printed on ceramic substrates (3.4×1.0 cm). The working electrode was composed of PB/carbon ink (disk-shaped, 4 mm diameter) and the counter electrode was carbon ink, whereas the pseudoreference electrode and electric contacts were silver. A small number of Fe_3O_4@pDA150/Gox nanoparticles were dispersed in PBS (50 μL), transferred onto the surface of the working electrode of DPR-700, and the supernatant was removed. This was done by keeping the DPR-700 horizontal and placing a neodymium magnet on the bottom part of the electrode to localize in a reproducible way the Fe_3O_4@pDA150/Gox nanoparticles onto the working surface, which thus avoided variations in the bead layer thickness or spreading area of the electrode surface between different measurements. To study the biosensor response against glucose concentration, a drop (≈50 μL) of glucose solutions with different concentrations were deposited onto the working, pseudoreference, and counter electrodes and a working potential of −150 mV was applied for 160 s. To measure the glucose concentration in blood samples, the blood samples were previously diluted in PBS (1:10). All experiments were performed at RT.

Quinone-Rich Fe_3O_4@pDA150/Gox Nanoparticles

Fe_3O_4 nanoparticles were prepared by using a chemical coprecipitation method under a N_2 atmosphere. $FeCl_3$ (3.24 g) and $FeSO_4 \cdot 7H_2O$ (2.78 g) were dissolved in aqueous HCl (200 mL, 1.2 mM) by ultrasound treatment. Then aqueous NaOH (300 mL, 1.25 M) was added dropwise under vigorous stirring over 30 min to form a black Fe_3O_4 precipitate. After vigorous stirring for another 30 min, the precipitate was magnetically decanted and washed thoroughly with ultrapure water until the supernatant solution reached neutrality (pH ≈7). For coating with pDA, Fe_3O_4 (500 mg) was dispersed in a solution of DA (25 mL, 10 mM) in PBS (pH 8.5) under continuous stirring for 3 h. After that, pDA-modified nanoparticles (Fe_3O_4@pDA) were magnetically decanted and washed thoroughly with ultrapure water to remove unreacted DA. The resulting black powder was heated in an oven at 150 °C for 1 h to oxidize the catechol groups to quinone groups, and a quinone-rich pDA film was obtained (Fe_3O_4@pDA150). Modified MNPs were then dispersed in water in an ultrasound bath for 30 min before further modifications. To immobilize the enzyme, Fe_3O_4@pDA150 (30 mg) was dispersed in a solution of Gox (1 mg mL^{-1}) in PBS (5 mL, pH 7.4) for 4 h under agitation at RT. The Gox-modified nanoparticles (Fe_3O_4@pDA150/Gox) were magnetically decanted and washed thoroughly with PBS to remove unreacted Gox, then further redispersed in PBS at a final concentration of 15 mg mL^{-1}. The enzyme-modified nanoparticles were kept at 4 °C until use. Fe_3O_4/Gox and Fe_3O_4@pDA/Gox-modified MNPs were prepared and compared against our optimized configuration. The amount of Gox bound in the different MNPs was determined from the difference between the initial and residual Gox found in the solution after immobilization. The band adsorption of Gox at $\lambda = 450$ nm was used in this study. Isolated pDA was obtained under the same conditions by using a reaction time of 24 h for further characterization studies. Finally, pDA was washed three times with double-distilled water and dried overnight at 40 °C.

Acknowledgements

The funds for the development of this device have been provided by subprograma INNCORPORA-MINECO (IPT-2012-0961-300000), Ministerio de Ciencia e Innovación (TIN2011-28146 and CTQ2011-24784), and the RECUPERA 2020 project of the Ministry of Economy and Competitiveness, Spain. We thank Dr. Reynaldo Villalonga (Department of Analytical Chemistry, Faculty of Chemistry, Complutense University of Madrid) for help with the HRTEM measurements.

Keywords: biosensors · glucose oxidase · magnetic properties · nanoparticles · natural products

[1] A. Bumb, S. K. Sarkar, N. Billington, M. W. Brechbiel, K. C. Neuman, *J. Am. Chem. Soc.* **2013**, *135*, 7815–7818.
[2] J. Choi, P. Schattling, F. D. Jochum, J. Pyun, K. Char, P. Theato, *J. Polym. Sci. Part A* **2012**, *50*, 4010–4018.
[3] S. Jiang, K. Y. Win, S. Liu, C. P. Teng, Y. Zheng, M.-Y. Han, *Nanoscale* **2013**, *5*, 3127–3148.
[4] X. Dong, X. Lu, K. Zhang, Y. Zhang, *Microchim. Acta* **2013**, *180*, 101–108.
[5] J. Zhang, W. Zhang, T. Bao, Z. Chen, *Analyst* **2014**, *139*, 242–250.
[6] L.-P. Zhu, J.-H. Jiang, B.-K. Zhu, Y.-Y. Xu, *Colloids Surf. B* **2011**, *86*, 111–118.
[7] J. Ryu, S. H. Ku, H. Lee, C. B. Park, *Adv. Funct. Mater.* **2010**, *20*, 2132–2139.
[8] R. Salgado, R. del Rio, M. A. del Valle, F. Armijo, *J. Electroanal. Chem.* **2013**, *704*, 130–136.
[9] B. M. Teo, R. van der Westen, L. Hosta-Rigau, B. Städler, *Biochim. Biophys. Acta Gen. Subj.* **2013**, *1830*, 4838–4847.
[10] V. K. Gupta, M. L. Yola, N. Özaltın, N. Atar, Z. Üstündağ, L. Uzun, *Electrochim. Acta* **2013**, *112*, 37–43.
[11] T. Gong, B. J. Adzima, N. H. Baker, C. N. Bowman, *Adv. Mater.* **2013**, *25*, 2024–2028.
[12] T. Date, T. Sawada, T. Serizawa, *Soft Matter* **2013**, *9*, 3469–3472.
[13] K. Ariga, J. P. Hill, Q. Ji, *Phys. Chem. Chem. Phys.* **2007**, *9*, 2319–2340.
[14] S. Srivastava, N. A. Kotov, *Acc. Chem. Res.* **2008**, *41*, 1831–1841.
[15] L. Wang, S. Guo, X. Hu, S. Dong, *Colloids Surf. A* **2008**, *317*, 394–399.
[16] A. Jaiswal, J. Colins, B. Agricole, P. Delhaes, S. Ravaine, *J. Colloid Interface Sci.* **2003**, *261*, 330–335.
[17] Y. Wei, N. Zhang, Y. Li, G. Shi, L. Jin, *Chin. J. Chem.* **2010**, *28*, 2489–2493.
[18] W.-H. Zhou, C.-H. Lu, X.-C. Guo, F.-R. Chen, H.-H. Yang, X.-R. Wang, *J. Mater. Chem.* **2010**, *20*, 880–883.
[19] H. Lee, S. M. Dellatore, W. M. Miller, P. B. Messersmith, *Science* **2007**, *318*, 426–430.
[20] H. Lee, J. Rho, P. B. Messersmith, *Adv. Mater.* **2009**, *21*, 431–434.
[21] M. E. Lynge, R. van der Westen, A. Postma, B. Stadler, *Nanoscale* **2011**, *3*, 4916–4928.
[22] J. B. Wood, M. W. Szyndler, A. R. Halpern, K. Cho, R. M. Corn, *Langmuir* **2013**, *29*, 10868–10873.
[23] X. Liu, J. Cao, H. Li, J. Li, Q. Jin, K. Ren, J. Ji, *ACS Nano* **2013**, *7*, 9384–9395.
[24] K.-J. Huang, L. Wang, H.-B. Wang, T. Gan, Y.-Y. Wu, J. Li, Y.-M. Liu, *Talanta* **2013**, *114*, 43–48.
[25] C. Rodriguez-Emmenegger, C. M. Preuss, B. Yameen, O. Pop-Georgievski, M. Bachmann, J. O. Mueller, C. Barner-Kowollik, *Adv. Mater.* **2013**, *25*, 6123–6127.
[26] R. Gu, W. Z. Xu, P. A. Charpentier, *J. Polym. Sci. Part A* **2013**, *51*, 3941–3949.
[27] C. Ruan, W. Shi, H. Jiang, Y. Sun, X. Liu, X. Zhang, Z. Sun, L. Dai, D. Ge, *Sens. Actuators B* **2013**, *177*, 826–832.
[28] Y. Fu, P. Li, Q. Xie, X. Xu, L. Lei, C. Chen, C. Zou, W. Deng, S. Yao, *Adv. Funct. Mater.* **2009**, *19*, 1784–1791.

[29] H.-P. Peng, R.-P. Liang, L. Zhang, J.-D. Qiu, *Biosens. Bioelectron.* **2013**, *42*, 293 – 299.
[30] Y. Wang, L. Liu, M. Li, S. Xu, F. Gao, *Biosens. Bioelectron.* **2011**, *30*, 107 – 111.
[31] Y. Wang, D. Zhang, Y. Wang, P. Qi, B. Hou, *Biosens. Bioelectron.* **2011**, *26*, 2595 – 2600.
[32] G. Wang, H. Huang, G. Zhang, X. Zhang, L. Wang, *Anal. Methods* **2011**, *3*, 2475 – 2477.
[33] J. Liebscher, R. Mrówczyński, H. A. Scheidt, C. Filip, N. D. Hădade, R. Turcu, S. Beck, *Langmuir* **2013**, *29*, 10539 – 10548.
[34] D. R. Dreyer, D. J. Miller, B. D. Freeman, D. R. Paul, C. W. Bielawski, *Langmuir* **2012**, *28*, 6428 – 6435.
[35] D. R. Dreyer, D. J. Miller, B. D. Freeman, D. R. Paul, C. W. Bielawski, *Chem. Sci.* **2013**, *4*, 3796 – 3802.
[36] Y. Liu, K. Ai, L. Lu, *Chem. Rev.* **2014**, *114*, 5057 – 5115.
[37] E. Faurea, C. Falentin-Daudréa, C. Jérômea, J. Lyskawab, D. Fournierb, P. Woiselb, C. Detrembleura, *Prog. Polym. Sci.* **2013**, *38*, 236 – 270.
[38] G. Wang, H. Huang, G. Zhang, X. Zhang, B. Fang, L. Wang, *Langmuir* **2011**, *27*, 1224 – 1231.
[39] H.-P. Peng, Y. Hu, A.-L. Liu, W. Chen, X.-H. Lin, X.-B. Yu, *J. Electroanal. Chem.* **2014**, *712*, 89 – 95.
[40] M. Lin, Y. Liu, X. Chen, S. Fei, C. Ni, Y. Fang, Q. Cai, *Biosens. Bioelectron.* **2013**, *45*, 82 – 88.
[41] G. Loget, J. B. Wood, K. Cho, A. R. Halpern, R. M. Corn, *Anal. Chem.* **2013**, *85*, 9991 – 9995.
[42] R. Luo, L. Tang, J. Wang, Y. Zhao, Q. Tu, Y. Weng, N. Huang, *Colloids Surf. B* **2013**, *106*, 66 – 73.
[43] J. M. Pingarrón, P. Yañez-Sedeño, A. González-Cortés, *Electrochim. Acta* **2008**, *53*, 5848 – 5866.
[44] A. Wittstock, J. Biener, J. Erlebacher, M. Bäumer, *Nanoporous Gold*, RSC, London, **2012**, pp. 167 – 198.
[45] H. C. Zhou, W. Li, Q. H. Shou, H. S. Gao, P. Xu, F. L. Deng, H. Z. Liu, *Chin. J. Chem. Eng.* **2012**, *20*, 146 – 151.
[46] Z. X. Zhang, Z. J. Wang, X. L. Wang, X. R. Yang, *Sens. Actuators B* **2010**, *147*, 428 – 433.
[47] C. Guo, Y. H. Ma, P. F. Su, B. S. Fang, *Biochem. Eng. J.* **2012**, *67*, 120 – 125.
[48] B. Kalska-Szostko, M. Rogowska, A. Dubis, K. Szymański, *Appl. Surf. Sci.* **2012**, *258*, 2783 – 2787.
[49] I. Mahmood, I. Ahmad, G. Chen, H. Z. Liu, *Biochem. Eng. J.* **2013**, *73*, 72 – 79.
[50] I. Willner, R. Baron, B. Willner, *Biosens. Bioelectron.* **2007**, *22*, 1841 – 1852.
[51] I. Willner, B. Willner, E. Katz, *Bioelectrochemistry* **2007**, *70*, 2 – 11.
[52] M. Martín, P. Salazar, R. Villalonga, S. Campuzano, J. M. Pingarron, J. L. Gonzalez-Mora, *J. Mater. Chem. B* **2014**, *2*, 739 – 746.
[53] W. L. Xia, N. Ma, *Biomass Bioenergy* **2010**, *34*, 890 – 896.
[54] J. Jordan, C. S. S. R. Kumar, C. Theegala, *J. Mol. Catal. B* **2011**, *68*, 139 – 146.
[55] H. E. Ghandoor, H. M. Zidan, M. M. H. Khalil, M. I. M. Ismail, *Int. J. Electrochem. Sci.* **2012**, *7*, 5734 – 5745.
[56] L. Zhuo, Y. Wu, L. Wang, J. Ming, Y. Yu, X. Zhang, F. Zhao, *J. Mater. Chem. A* **2013**, *1*, 3954 – 3960.
[57] X. Teng, D. Black, N. J. Watkins, Y. Gao, H. Yang, *Nano Lett.* **2013**, *13*, 261 – 264.
[58] M. Gao, W. Li, J. Dong, Z. Zhang, B. Yang, *World J. Condens. Matter Phys.* **2011**, *1*, 49 – 54.
[59] W. Chen, Z. Fan, X. Pan, X.; Bao, *J. Am. Chem. Soc.* **2008**, *130*, 9414 – 9419; X. Bao, *J. Am. Chem. Soc.* **2008**, *130*, 9414 – 9419.
[60] L. Yan, Y. B. Zheng, F. Zhao, S. Li, X. Gao, B. Xu, P. S. Weiss, Y. Zhao, *Chem. Soc. Rev.* **2012**, *41*, 97 – 114.
[61] N. Domingo, E. Bellido, D. Ruiz-Molina, *Chem. Soc. Rev.* **2012**, *41*, 258 – 302.
[62] S. Singamaneni, V. N. Bliznyuk, C. Binek, E. Y. Tsymbal, *J. Mater. Chem.* **2011**, *21*, 16819 – 16845.
[63] A. G. Orive, A. H. Creus, D. Grumelli, G. A. Benitez, L. Andrini, F. G. Requejo, C. Bonazzola, R. C. Salvarezza, *J. Phys. Chem. C* **2009**, *113*, 17097 – 17103.
[64] M. F. Calderón, E. Zelaya, G. A. Benitez, P. L. Schilardi, A. H. Creus, A. G. Orive, R. C. Salvarezza, F. J. Ibáñez, *Langmuir* **2013**, *29*, 4670 – 4678.
[65] R. B. Frankel, *Annu. Rev. Biophys. Bioeng.* **1984**, *13*, 85 – 103.
[66] S. Schreiber, M. Savla, D. V. Pelekhov, D. F. Iscru, C. Selcu, P. C. Hammel, G. Agarwal, *Small* **2008**, *4*, 270 – 278.
[67] V. F. Puntes, P. Gorostiza, D. M. Aruguete, N. G. Bastus, A. P. Alivisatos, *Nat. Mater.* **2004**, *3*, 263 – 268.
[68] F. Yu, S. Chen, Y. Chen, H. Li, L. Yang, Y. Chen, Y. Yin, *J. Mol. Struct.* **2010**, *982*, 152 – 161.
[69] C. Cheng, S. Li, W. Zhao, Q. Wei, S. Nie, S. Sun, C. Zhao, *J. Membr. Sci.* **2012**, *417 – 418*, 228 – 236.
[70] P. Salazar, M. Martín, R. Roche, R. D. O'Neill, J. L. González-Mora, *Electrochim. Acta* **2010**, *55*, 6476 – 6484.
[71] P. Salazar, M. Martín, R. D. O'Neill, R. Roche, J. L. González-Mora, *Colloids Surf. B* **2012**, *92*, 180 – 189.
[72] P. Salazar, M. Martín, R. D. O'Neill, R. Roche, J. L. González-Mora, *J. Electroanal. Chem.* **2012**, *674*, 48 – 56.
[73] P: Salazar, M. Martín, R. Roche, J. L. González-Mora, R. D. O'Neill, *Biosens. Bioelectron.* **2010**, *26*, 748 – 753.
[74] H. N. Bhatti, N. Saleem, *Food Technol. Biotechnol.* **2009**, *47*, 331 – 335.
[75] E. O. Odebunmi, S. O. Owalude, *J. Appl. Sci. Environ. Manage.* **2007**, *11*, 95 – 100.
[76] Z. Dai, M. Fang, J. Bao, H. Wang, T. Lu, *Anal. Chim. Acta* **2007**, *591*, 195 – 199.
[77] D. Pan, J. Chen, S. Yao, W. Tao, L. Nie, *Anal. Sci.* **2005**, *21*, 367 – 371.
[78] S. Cosnier, F. Lambert, M. Stoytcheva, *Electroanalysis* **2000**, *12*, 356 – 360.
[79] X. Wei, T. Liu, J. Li, X. Chen, *Int. J. Electrochem. Sci.* **2011**, *6*, 4953 – 4966.
[80] B. E. P. Swoboda, V. Massay, *J. Biol. Chem.* **1965**, *240*, 2209 – 2215.
[81] C. Mousty, B. Galland, S. Cosnier, *Electroanalysis* **2001**, *13*, 186 – 190.
[82] K. I. Ozoemena, T. Nyokong, *Electrochim. Acta* **2006**, *51*, 5131 – 5136.
[83] Z. Wang, S. Liu, P. Wu, C. Cai, *Anal. Chem.* **2009**, *81*, 1638 – 1645.

Received: June 10, 2014
Revised: July 17, 2014
Published online on September 5, 2014